Helicity-Changing Brillouin Light Scattering by Magnons in a Ferromagnetic Crystal

R. Hisatomi,[1,*] A. Noguchi,[2] R. Yamazaki,[1] Y. Nakata,[1] A. Gloppe,[1] Y. Nakamura,[1,3] and K. Usami[1,†]
[1]Research Center for Advanced Science and Technology (RCAST), The University of Tokyo, Meguro-ku, Tokyo 153-8904, Japan
[2]Komaba Institute for Science (KIS), The University of Tokyo, Meguro-ku, Tokyo 153-8904, Japan
[3]Center for Emergent Matter Science (CEMS), RIKEN, Wako, Saitama 351-0198, Japan

(Received 10 May 2019; published 12 November 2019)

Brillouin light scattering in ferromagnetic materials usually involves one magnon and two photons and their total angular momentum is conserved. Here, we experimentally demonstrate the presence of a helicity-changing two-magnon Brillouin light scattering in a ferromagnetic crystal, which can be viewed as a four-wave mixing process involving two magnons and two photons. Moreover, we observe an unconventional helicity-changing one-magnon Brillouin light scattering, which apparently infringes the conservation law of the angular momentum. We show that the crystal angular momentum intervenes to compensate the missing angular momentum in the latter scattering process.

DOI: 10.1103/PhysRevLett.123.207401

For all the physical processes under the continuous rotational symmetry, the angular momentum is a good quantum number: it can only take quantized values, i.e., integers multiplied by the fundamental constant $\hbar$. Under such circumstances, the angular momentum is transferred from one agent to the other in such a way that the total amount is conserved. The angular momentum transfer occupies a central place in the modern development of spintronics. For example, spin pumping [1], spin transfer torque [2], and the spin Hall effect [3] enable us to transfer angular momentum from electric currents to magnetization and vice versa.

Angular momentum transfer occurs not only between spin-polarized electric current and magnetization, but also between polarized light and magnetization. With magneto-optical effects such as the Faraday effect and the Cotton-Mouton effect, the coupling between polarized light and magnetization can be realized. Since at optical frequencies the magnetic dipole interaction ceases to play any role, the electric dipole moment associated with the magnetization instead dictates the magneto-optical effects [4,5], which microscopically arise due to the (generally weak) spin-orbit coupling.

To investigate a further possibility of the magneto-optical effect in manipulating magnetization dynamics, let us turn our attention to the electric quadrupole moment. For ferromagnetic (and ferrimagnetic) materials there has been much less interest in the electric quadrupole moment [6], which would manifest itself in a process of a helicity-changing Brillouin light scattering in the Faraday geometry (namely, light propagates parallel to the external magnetic field) as we discuss here. This is in stark contrast to the familiar one-magnon Brillouin light scattering in the Voigt geometry (namely, the light propagates perpendicular to the external magnetic field), around which the emergent field of cavity optomagnonics [7–14] is revolving. Nevertheless, for antiferromagnetic materials it is well known that the Brillouin light scattering by the quadrupole moment associated with two-magnon excitations is large when the two magnons involved in the scattering process originate in the modes with large and opposite wave numbers [15–19]. In atomic physics, quadrupole moments of collective spin states have been widely studied [20–23] in connection with spin squeezing [24].

In this Letter, with a ferromagnetic spherical crystal, we experimentally explore the Brillouin light scattering in Faraday geometry using polarization-sensitive optical heterodyne measurements [7,12]. It is revealed that two-magnon excitations induce electric quadrupole moments, which give rise to the helicity-changing Brillouin light scattering. Besides, we find an unconventional helicity-changing Brillouin light scattering which only involves one-magnon excitations. For the latter case the conservation of the angular momentum is upheld only when the crystal angular momentum [25–29] is taken into account. The possible relevance to the elusive rotational Doppler effect [25] in the context of magnon-induced Brillouin light scattering is also discussed.

The experimental setup is schematically shown in Figs. 1(a) and 1(b). A spherical crystal (0.5-mm in diameter) of yttrium iron garnet (YIG) is attached to an alumina rod oriented along the crystal axis $\langle 110 \rangle$ and placed at the center of the gap of a magnetic circuit as shown in Fig. 1(a). The YIG sphere can be rotated about the $\langle 110 \rangle$ crystal axis, which allows us to apply a static magnetic field along either $\langle 100 \rangle$, $\langle 111 \rangle$, or any orientation in the (110) plane. The magnetic field, created by the magnetic circuit, around 130 kA/m saturates the magnetization of the YIG sphere along the z axis and can be varied. A coupling loop coil above the YIG sphere generates an

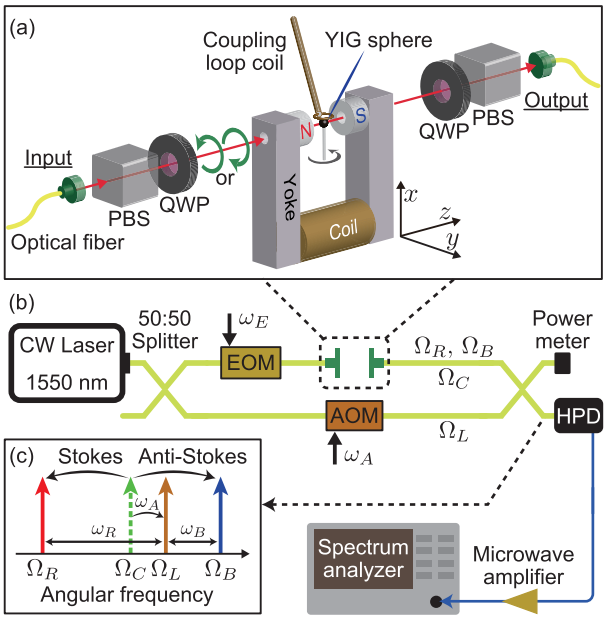

FIG. 1. (a) A spherical crystal (0.5 mm in diameter) of yttrium iron garnet is placed in the gap of a magnetic circuit which consists of a pair of cylindrical permanent magnets, a coil, and a yoke. A coupling loop coil above the YIG sphere is used to excite magnons. By a set of a quarter-wave plate and a polarization beam splitter either left or right circularly polarized light is chosen for the input and the output. (b) Light from a cw laser is separated into two paths by an optical fiber splitter. An electro-optic modulator (EOM) in the upper path is used to calibrate signals and an acousto-optic modulator in the lower path is used to generate a local oscillator. The signal and the LO are combined and the resultant signal is sent to a power meter and a high-speed photo detector followed by a spectrum analyzer after a microwave amplifier. (c) Schematic representation of the relevant frequencies. The carrier light at Ω_C is scattered into the sidebands at Ω_R and Ω_B. The beat signals appear at ω_R and ω_B with respect to the LO at Ω_L.

oscillating magnetic field perpendicular to the saturated magnetization M_z to excite magnons in the uniformly oscillating magnetostatic mode (Kittel mode) giving rise to the time-varying transverse magnetizations $M_x(t)$ and $M_y(t)$.

Figures 2(a) and 2(b) show the microwave reflection spectra indicating the ferromagnetic resonances for the external magnetic field $\boldsymbol{H}_{\rm ext}$ being parallel to the $\langle 100\rangle$ and $\langle 111\rangle$ axes, respectively. From the fitting we obtain the resonance frequency of the Kittel mode $\omega_K/2\pi = 5.07$ GHz for $\boldsymbol{H}_{\rm ext}\|\langle 100\rangle$ and $\omega_K/2\pi = 5.21$ GHz for $\boldsymbol{H}_{\rm ext}\|\langle 111\rangle$. Depending on the direction $\boldsymbol{H}_{\rm ext}$ with respect to the crystal axis, the magnon resonance angular frequency ω_K varies due to the magnetocrystalline anisotropy [30,31], which is used to determine the crystal axis as described in the Supplemental Material [32].

We now explore the Brillouin light scattering under the condition in which the Kittel mode is continuously driven at the resonance. As shown in Fig. 1(b) a cw laser light with a wavelength of 1550 nm (the angular frequency of Ω_C) is split into two paths by an optical fiber splitter. The light in the lower path acts as a local oscillator (LO) whose frequency is shifted by $\omega_A/2\pi = 80$ MHz from Ω_C by an acousto-optic modulator (AOM). In the upper path, the laser light is sent through the YIG sphere along the z axis. In this Faraday geometry, the discrete rotational symmetry is assured along the z axis: for the case of $\boldsymbol{H}_{\rm ext}\|\langle 100\rangle$ it is fourfold symmetry, and for the case of $\boldsymbol{H}_{\rm ext}\|\langle 111\rangle$ it is threefold symmetry. By a pair of a quarter-wave plate (QWP) and a polarization beam splitter (PBS) before and after the YIG sphere as shown in Fig. 1(a), either the left or right circularly polarized light can be selected as the input and the output. The scattered light from the upper path interferes with the LO light from the lower path after the second optical fiber splitter so that the resultant beat signals originating from the Stokes scattering (red sideband) and the anti-Stokes scattering (blue sideband) appear at different angular frequencies, ω_R and ω_B, respectively, as schematically shown in Fig. 1(c). These beat signals are detected by a high-speed photodetector (HPD) and then amplified and analyzed by a spectrum analyzer. By using this setup we can investigate the selection rule both in the helicity-conserving and the helicity-changing Brillouin light scattering.

Figure 2(c) shows the observed two-magnon scattering efficiencies for the case of $\boldsymbol{H}_{\rm ext}\|\langle 100\rangle$. The scattering efficiencies are deduced from the signal at the angular frequency of $\omega_R = 2\omega_K + \omega_A$ for the two-magnon Stokes sideband and that at $\omega_B = 2\omega_K - \omega_A$ for the two-magnon anti-Stokes sideband [see Supplemental Material [32] for a part of the raw data used to deduce the scattering efficiencies. The calibration scheme is also provided in Ref. [32]. The same comment is applied to other scattering efficiencies shown in Figs. 2(d), 2(e), and 2(f)]. The significant helicity-changing two-magnon Stokes sideband appears when the input (output) polarization is left (right) circular ($L_i \to R_o$ configuration), while the significant helicity-changing two-magnon anti-Stokes sideband appears when the input (output) polarization is right (left) circular ($R_i \to L_o$ configuration). The fact that there is no signal when the microwave drive angular frequency is detuned from the resonance of the Kittel mode by $\delta\omega$ ($\delta\omega > \gamma_t$, where $\gamma_t \sim 2\pi \times 8$ MHz is the linewidth of the Kittel mode) ensures the absence of the spurious drive signal coupled directly into the HPD.

As described in the Supplemental Material [32], the scattering efficiency for the helicity-changing two-magnon Stokes sideband at ω_R is proportional to the square of the electric quadrupole moment, $-\alpha M_-(t)^2$, in the $L_i \to R_o$ configuration, where $M_-(t) = M_x(t) - iM_y(t)$ is the transverse magnetization of the Kittel mode and $\alpha = (G_{11}/4) - (G_{12}/4) + (G_{44}/2)$ with G_{11}, G_{12}, and G_{44} are three parameters that specify the dielectric tensor of the cubic crystal (here, YIG). The scattering efficiency for the

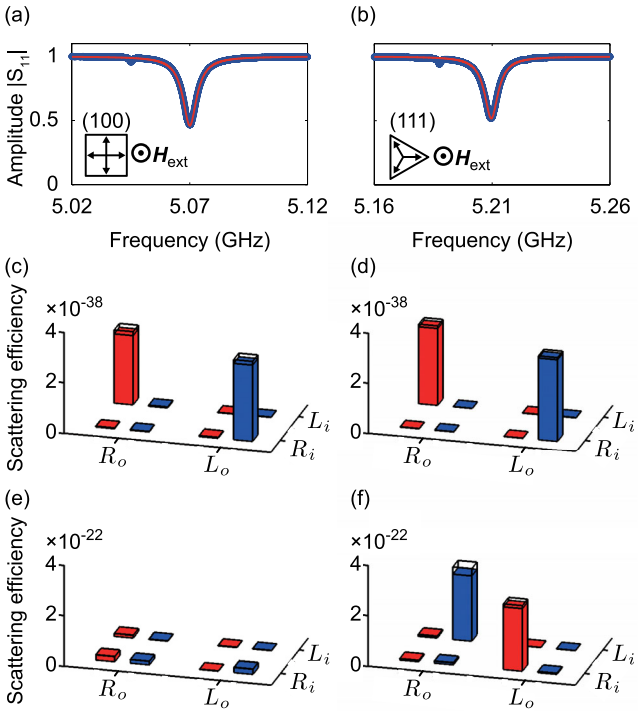

FIG. 2. (a) and (b): Microwave reflection spectrum for the Kittel mode under the external magnetic fields (a) $\boldsymbol{H}_{\text{ext}}\|\langle 100\rangle$ and (b) $\boldsymbol{H}_{\text{ext}}\|\langle 111\rangle$. The blue points show the measured reflection amplitude whereas the red curve shows the Lorentzian fitting. (c)–(f): Scattering efficiencies of the Stokes sideband (red bars) and the anti-Stokes sideband (blue bars) by two magnons [(c),(d)] and one magnon [(e),(f)] for four distinct polarization sets under $\boldsymbol{H}_{\text{ext}}\|\langle 100\rangle$ [(c),(e)] and $\boldsymbol{H}_{\text{ext}}\|\langle 111\rangle$ [(d),(f)]. The height of the color bar shows the mean scattering efficiency and the difference between the top of the black wire frame and the bar represents a standard deviation estimated from measurements repeated six times. R_i (L_i) represents the right-circular (left-circular) polarization for the input field, while R_o (L_o) represents right-circular (left-circular) polarization for the output field.

helicity-changing two-magnon anti-Stokes sideband at ω_B can be similarly explained with the electric quadrupole moment, $-\alpha M_+(t)^2$, with $M_+(t) = M_x(t) + iM_y(t)$. Note that in the quantum mechanical picture $M_-(t)^2$ [$M_+(t)^2$] corresponds to an operator which creates (annihilates) a pair of magnons [32]. Thus the helicity-changing two-magnon Brillouin light scattering can be viewed as a four-wave mixing process involving two magnons and two photons, which has been largely neglected. Note here that the Kittel mode with zero wave number is diametrically opposed to the modes with large wave numbers by which the four-wave mixing process involving two magnons and two photons has previously been observed with antiferromagnetic materials [15–19].

To gain further insight, we now turn our attention to the case in which $\boldsymbol{H}_{\text{ext}}\|\langle 111\rangle$. Figure 2(d) shows the observed helicity-changing and the helicity-conserving two-magnon scattering efficiencies for the case of $\boldsymbol{H}_{\text{ext}}\|\langle 111\rangle$. As in the case of $\boldsymbol{H}_{\text{ext}}\|\langle 100\rangle$, the significant Stokes sideband again appears in the $L_i \to R_o$ configuration while the significant anti-Stokes sideband appears in the $R_i \to L_o$ configuration. These sideband generation efficiencies agree with the ones theoretically predicted [32], which are proportional to the squares of the respective electric quadrupole moments, $-\beta M_-(t)^2$ and $-\beta M_+(t)^2$, with $\beta = (G_{11}/6) - (G_{12}/6) + (2G_{44}/3)$, respectively. To see the situation schematically, Fig. 3 shows the energy-level diagrams relevant to the Brillouin scattering. The states $|g\rangle$ and $|e\rangle$ describe the electronic ground and excited states relevant to the dominant optical transition. Under the static magnetic field those states split to form a ladder depending on the magnon number, which is denoted by $|n\rangle$. Here, the helicity-changing two-magnon Stokes sideband in the $L_i \to R_o$ configuration observed in Fig. 2(d), for instance, corresponds to the transition that connects $|g,n-1\rangle$ and $|g,n+1\rangle$ in Fig. 3. In this transition, the angular momentum gained by light is $\Delta J_p = 2\hbar$, while the same amount of angular momentum is lost from the sphere (i.e., $\Delta J_m = -2\hbar$) by creating two magnons (increasing magnon reduces the angular momentum of the sphere). Here, the total angular momenta are conserved among relevant two photons and two magnons and $\Delta J_p + \Delta J_m = 0$.

In the case of $\boldsymbol{H}_{\text{ext}}\|\langle 111\rangle$ a unusual situation appears when the scattering involves two photons and one magnon, where the conservation of angular momentum is seemingly broken. As in the case of the two-magnon Brillouin light scattering, we obtain the one-magnon scattering efficiencies deduced from the signal observed at the angular frequency of $\omega_R = \omega_K + \omega_A$ for the Stokes sideband and that at $\omega_B = \omega_K - \omega_A$ for the anti-Stokes sideband, which are shown in Figs. 2(e) and 2(f). In the case of $\boldsymbol{H}_{\text{ext}}\|\langle 100\rangle$, there is indeed no noticeable scattering as shown in Fig. 2(e). In the case of $\boldsymbol{H}_{\text{ext}}\|\langle 111\rangle$, however, the significant helicity-changing Stokes sideband appears in the

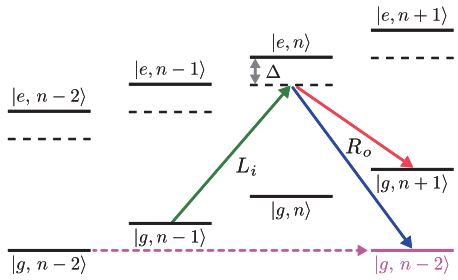

FIG. 3. Energy-level diagrams relevant to the Brillouin scattering. The states are labeled by the electronic ground and excited states $|g\rangle$ and $|e\rangle$, respectively, with the number of magnons as $|n\rangle$. The green arrows represent the input carrier with the angular frequency of Ω_C and the red and blue arrows represent the Stokes and anti-Stokes sidebands with Ω_R and Ω_B, respectively, for the $L_i \to R_o$ configuration. Δ denotes the frequency detuning between the light and the $|g\rangle \leftrightarrow |e\rangle$ transition. The horizontal dashed arrow connects the identical states due to the ambiguity emerged from the crystal angular momentum $3\hbar$.

$R_i \to L_o$ configuration, and the significant helicity-changing anti-Stokes sideband appears in the $L_i \to R_o$ configuration as shown in Fig. 2(f). This helicity-changing one-magnon anti-Stokes sideband generation in the $L_i \to R_o$ configuration, for instance, corresponds to the transition that connects $|g, n-1\rangle$ and $|g, n-2\rangle$ in Fig. 3, where the angular momentum gained in the sphere by annihilating one magnon is $\Delta J_m = \hbar$, even though the light also gains the angular momentum by $\Delta J_p = 2\hbar$.

The key to save the conservation of angular momentum is the crystal angular momentum associated with the threefold symmetry possessed by the crystal along $\boldsymbol{H}_{\rm ext} \| \langle 111 \rangle$. Unlike isolated atoms, liquids, or amorphous solids, crystals do not have the continuous rotational symmetry and thus the angular momentum is not a good quantum number. Angular momentum transfer processes taking place in the crystals are then determined up to the crystal angular momentum. This situation is analogous to the one that the linear momentum of an electron in the crystal has an ambiguity of $\hbar$ times reciprocal lattice vectors. In our particular example of the cubic crystal with $\boldsymbol{H}_{\rm ext} \| \langle 111 \rangle$, the crystal angular momentum is an integer multiple of $3\hbar$. With this in mind, let us revisit the transition that connects $|g, n-1\rangle$ and $|g, n-2\rangle$ in Fig. 3. The total angular momentum $3\hbar$ gained by the sphere and the light can indeed be identified to be zero because of the ambiguity emerged from the crystal angular momentum $3\hbar$ as indicated in Fig. 3.

These processes can thus be understood as a result of rotational analog of the umklapp process due to the crystal angular momentum. Note that in the standard group-theoretic analysis of selection rules in an inelastic scattering, everything is boiled down to the analysis of the excitation of the scatterer as a whole in terms of the irreducible representations of its symmetry group [43,44]. Thus, the origin of the angular momentum of the excitation (either coming from the one of magnetization or that of crystal, in our particular example) is usually not questioned. The importance of the crystal angular momentum has been argued in connection with the second harmonic generation [25,26,29], parametric down-conversion [27], and the Raman scattering by magnons with THz eigenfrequency in an antiferromagnetic material [28].

The fully continuous rotational symmetry for the Brillouin light scattering processes can be recovered if the rotational degree of freedom for the crystalline sphere as a whole is liberated. This can be done by considering the sphere as a freely rotating rigid body and introducing the azimuthal angle ϕ for the sphere along $\boldsymbol{H}_{\rm ext} \| \langle 111 \rangle$ [32]. The scattering efficiency of this sideband generation process now depends on ϕ and is proportional to the square of the electric quadrupole moment, $\xi M_+(t)$, with $\xi = (\sqrt{2}/3) e^{-3i\phi} g M_z$ as described in the Supplemental Material [32]. Here $g = G_{11} - G_{12} - 2G_{44}$, which is zero when the material is isotropic. The phase factor $e^{-3i\phi}$ in ξ can be considered as the spherical harmonics Y_3^{-3} denoting the rotation of the spherical crystal. By writing the matrix element of the one-magnon transition amplitude from $|g, n-1\rangle$ to $|g, n-2\rangle$ in Fig. 3 as $\mathcal{U}_o$, the angular momentum of the sphere acquired in the course of the transition can be given by $\Delta J_c = \mathrm{Tr}[\hat{\rho}(\mathcal{U}_o^\dagger \hat{L}_z \mathcal{U}_o - \hat{L}_z)] = -3\hbar$ [25,32], where $\hat{\rho}$ is the density matrix for the rotational state of the sphere and $\hat{L}_z$ is the z component of the angular momentum operator for the sphere, whose Euler-angle representation reads $-i\hbar(\partial/\partial\phi)$. Thus, the excess angular momentum $\Delta J_m + \Delta J_p = 3\hbar$ seen in the transition from $|g, n-1\rangle$ to $|g, n-2\rangle$ in Fig. 3 is indeed retrieved as the rotation of the sphere, leading to $\Delta J_m + \Delta J_p + \Delta J_c = 0$. On the other hand, the matrix element of the two-magnon transition amplitude from $|g, n-1\rangle$ to $|g, n+1\rangle$ in Fig. 3 does not depend on ϕ, meaning that there is no rotation of the sphere in this transition. The similar conclusion holds for other angular momentum transfers. We emphasize that the threefold discrete rotational symmetry of crystal is engraved deeply even when the full continuous rotational symmetry is resumed by liberating the rotational degree of freedom of the crystal.

The nontrivial phase factor $e^{-3i\phi}$ in ξ would give rise to an additional observable consequence: when the sphere is rotating along $\boldsymbol{H}_{\rm ext} \| \langle 111 \rangle$ at the angular velocity of ω_L the resultant sideband as a result of the one-magnon transition would experience the rotational Doppler shift by $\Delta\omega_K = -3 \times \omega_L$. Here, the factor -3 stems from $e^{-3i\phi}$ and is basically what Simon and Bloembergen have predicted as early as in 1968 in the context of second harmonic generation [25]. The predicted rotational Doppler shift has, to the best of our knowledge, not yet been observed. We envision that observing this shift in the magnon-induced Brillouin light scattering is feasible once a sphere is enforced to rotate uniformly or levitated to set free the rotation. We note that the levitation of a micron-scale ferromagnetic particles has been recently demonstrated [45,46].

In our experiment, the sphere is rigidly fixed on the optical table and the resultant moment of inertia is enormous. Since the rotational kinetic energy of the sphere acquired by the torque associated with the scattering is thus negligibly small, the intervention of the crystal angular momentum in the Brillouin light scattering would not affect the phase relationship between the input light and the scattered output light. As shown in the Supplemental Material [32], a set of measurements reveals that the phase relationship indeed remains unimpaired.

In summary, we demonstrated the presence of helicity-changing two-magnon scattering as well as the helicity-changing crystal-angular-momentum-assisted one-magnon scattering. We anticipate that the former process is ubiquitous in any ferro- and ferrimagnetic insulating materials supporting long wavelength magnetostatic modes. The latter process, however, only occurs in such materials with crystalline structure having threefold symmetry along the external magnetic field $\boldsymbol{H}_{\rm ext}$ in the Faraday geometry.

We would like to thank Y. Tabuchi, S. Kono, A. Okada, A. Osada, G. E. W. Bauer, K. Sato, T. Satoh, E. Saitoh, S. Daimon, A. Hatakeyama, H. Watanabe, A. Nunnenkamp, D. Malz, A. Ramsay, and J. Haigh for useful discussion. This work is partly supported by KAKENHI (Grant No. 26220601) and JST-ERATO project (Grant No. JPMJER1601).

*ryusuke.hisatomi@qc.rcast.u-tokyo.ac.jp
†usami@qc.rcast.u-tokyo.ac.jp

[1] M. Johnson and R. H. Silsbee, Phys. Rev. B **35**, 4959 (1987).
[2] D. C. Ralph and M. D. Stiles, J. Magn. Magn. Mater. **320**, 1190 (2008).
[3] J. Sinova, S. O. Valenzuela, J. Wunderlich, C. H. Back, and T. Jungwirth, Rev. Mod. Phys. **87**, 1213 (2015).
[4] L. D. Landau, E. M. Lifshitz, and L. P. Pitaevskii, *Electrodynamics of Continuous Media*, 2nd ed. (Butterworth-Heinenann, Oxford, England, 1984).
[5] P. S. Pershan, J. Appl. Phys. **38**, 1482 (1967).
[6] A. Kirilyuk, A. V. Kimel, and Th. Rasing, Rev. Mod. Phys. **82**, 2731 (2010).
[7] A. Osada, R. Hisatomi, A. Noguchi, Y. Tabuchi, R. Yamazaki, K. Usami, M. Sadgrove, R. Yalla, M. Nomura, and Y. Nakamura, Phys. Rev. Lett. **116**, 223601 (2016).
[8] X. Zhang, N. Zhu, C.-L. Zou, and H. X. Tang, Phys. Rev. Lett. **117**, 123605 (2016).
[9] J. A. Haigh, A. Nunnenkamp, A. J. Ramsay, and A. J. Ferguson, Phys. Rev. Lett. **117**, 133602 (2016).
[10] S. ViolaKusminskiy, H. X. Tang, and F. Marquardt, Phys. Rev. A **94**, 033821 (2016).
[11] S. Sharma, Y. M. Blanter, and G. E. W. Bauer, Phys. Rev. B **96**, 094412 (2017).
[12] A. Osada, A. Gloppe, R. Hisatomi, A. Noguchi, R. Yamazaki, M. Nomura, Y. Nakamura, and K. Usami, Phys. Rev. Lett. **120**, 133602 (2018).
[13] J. A. Haigh, N. J. Lambert, S. Sharma, Y. M. Blanter, G. E. W. Bauer, and A. J. Ramsay, Phys. Rev. B **97**, 214423 (2018).
[14] A. Osada, A. Gloppe, Y. Nakamura, and K. Usami, New J. Phys. **20**, 103018 (2018).
[15] P. A. Fleury, S. P. S. Porto, L. E. Cheesman, and H. J. Guggenheim, Phys. Rev. Lett. **17**, 84 (1966).
[16] P. A. Fleury, S. P. S. Porto, and R. Loudon, Phys. Rev. Lett. **18**, 658 (1967).
[17] T. Moriya, J. Phys. Soc. Jpn. **23**, 490 (1967).
[18] T. Moriya, J. Appl. Phys. **39**, 1042 (1968).
[19] P. A. Fleury and R. Loudon, Phys. Rev. **166**, 514 (1968).
[20] J. Hald, J. L. Sørensen, C. Schori, and E. S. Polzik, Phys. Rev. Lett. **83**, 1319 (1999).
[21] C. Gross, H. Strobel, E. Nicklas, T. Zibold, N. Bar-Gill, G. Kurizki, and M. K. Oberthaler, Nature (London) **480**, 219 (2011).
[22] B. Lücke, M. Scherer, J. Kruse, L. Pezzé, F. Deuretzbacher, P. Hyllus, O. Topic, J. Peise, W. Ertmer, J. Arlt, L. Santos, A. Smerzi, and C. Klempt, Science **334**, 773 (2011).
[23] C. D. Hamley, C. S. Gerving, T. M. Hoang, E. M. Bookjans, and M. S. Chapman, Nat. Phys. **8**, 305 (2012).
[24] M. Kitagawa and M. Ueda, Phys. Rev. A **47**, 5138 (1993).
[25] H. J. Simon and N. Bloembergen, Phys. Rev. **171**, 1104 (1968).
[26] N. Bloembergen, J. Opt. Soc. Am. **70**, 1429 (1980).
[27] J. Visser, E. R. Eliel, and G. Nienhuis, Phys. Rev. A **66**, 033814 (2002).
[28] T. Higuchi, N. Kanda, H. Tamaru, and M. Kuwata-Gonokami, Phys. Rev. Lett. **106**, 047401 (2011).
[29] K. Konishi, T. Higuchi, J. Li, J. Larsson, S. Ishii, and M. Kuwata-Gonokami, Phys. Rev. Lett. **112**, 135502 (2014).
[30] A. G. Gurevich and G. A. Melkov, *Magnetization Oscillations and Waves* (CRC Press, Boca Raton, 1996).
[31] D. D. Stancil and A. Prabhakar, *Spin Waves: Theory and Applications* (Springer, New York, 2009).
[32] See Supplemental Material at http://link.aps.org/supplemental/10.1103/PhysRevLett.123.207401 which includes Refs. [33–42] and details on the theory, the determination of the crystal axis, the calibration of scattering efficiencies, and experiments on coherence.
[33] D. Budker, D. F. J. Kimball, and D. DeMille, *Atomic Physics*, 2nd ed. (Oxford University Press, Oxford, England, 2008).
[34] L. D. Landau and E. M. Lifshitz, *Theory of Elasticity*, 3rd ed. (Butterworth-Heinenann, Oxford, England, 1986).
[35] J. F. Nye, *Physical Properties of Crystals* (Oxford University Press, Oxford, 1985).
[36] W. Happer and B. S. Mathur, Phys. Rev. **163**, 12 (1967).
[37] J. M. Geremia, J. K. Stockton, and H. Mabuchi, Phys. Rev. A **73**, 042112 (2006).
[38] K. Hammerer, A. S. Sørensen, and E. S. Polzik, Rev. Mod. Phys. **82**, 1041 (2010).
[39] C. Kittel, *The Quantum Theory of Solids* (Wiley, New York, 1963).
[40] C. Cohen-Tannoudji, J. Dupont-Roc, and G. Grynberg, *Atom-Photon Interactions* (John Wiley and Sons, New York, 1992).
[41] D. Healy Jr., Phys. Rev. **86**, 1009 (1952).
[42] A. A. Clerk, M. H. Devoret, S. M. Girvin, F. Marquardt, and R. J. Schoelkopf, Rev. Mod. Phys. **82**, 1155 (2010).
[43] M. Tinkham, *Group Theory and Quantum Mechanics* (McGraw-Hill, New York, 1964).
[44] W. Hayes and R. Loudon, *Scattering of Light by Crystals* (Wiley, New York, 1978).
[45] T. Wang, S. Lourette, S. R. OKelley, M. Kayci, Y. B. Band, Derek F. Jackson Kimball, A. O. Sushkov, and D. Budker, Phys. Rev. Applied **11**, 044041 (2019).
[46] P. Huillery, T. Delord, L. Nicolas, M. Van Den Bossche, M. Perdriat, and G. Hétet, arXiv:1903.09699.